ADVANCED FUNCTIONAL MATERIALS
www.afm-journal.de

Controlling Interfacial Reduction Kinetics and Suppressing Electrochemical Oscillations in $Li_4Ti_5O_{12}$ Thin-Film Anodes

Yue Chen, Handian Pan, Chun Lin, Jiaxin Li, Rongsheng Cai, Sarah J. Haigh, Guiying Zhao, Jianmin Zhang,* Yingbin Lin, Oleg V. Kolosov,* and Zhigao Huang**

Understanding the fundamentals of surface decoration effects in phase-separation materials, such as lithium titanate (LTO), is important for optimizing the lithium-ion battery (LIB) performance. LTO polycrystalline thin-film electrodes with and without doped Al–ZnO (AZO) surface coating decoration are used as ideal models to gain insights into the mechanisms involved. Operando shear force modulation spectroscopy is used to observe for the first time the nanoscale dynamics of solid-electrolyte-interphase (SEI) formation on the electrode surfaces, confirming that the AZO coating is electrochemically converted into a stiff, homogenous SEI layer that protects the surface from the electrolyte-induced decomposition. This AZO layer and its resultant artificial SEI-layer have higher Li-ion transport rates than the unmodified surface. These layers can reduce barriers to surface nucleation and facilitate rapid redistribution of lithium-ions during the $Li_4Ti_5O_{12} \rightleftarrows Li_7Ti_5O_{12}$ phase separation, significantly inhabiting the orderly collective phase-separation behavior (electrochemical oscillation) in the LTO electrode. The suppressed voltage oscillations indicate more homogeneous local exchange current density and de/intercalation states with the decorated electrodes, thereby extending their battery efficiency and long-term cycling stability. This work highlights the ultimate importance of surface treatment for LIB materials for determining their interfacial chemistry and phase transition during the intercalation/deintercalation.

1. Introduction

Interface modification has been demonstrated as the most effective strategy to improve electrode–electrolyte interfacial properties and compatibility,[1,2] by stabilizing the crystalline surface structure of the electrodes,[3] accelerating lithium-ions transportation through the electrode–electrolyte interfaces (EEIs),[4] and slowing solid-electrolyte-interphase (SEI) formation. Nonetheless, there has been no detailed investigation of the effects of surface-coatings on the phase-separation behavior in lithium titanium oxide (LTO) anode, which suffer from sluggish two-phase transition kinetics during lithiation/delithiation.[5,6]

Zhou's group reported for the first time statistically significant oscillations in the galvanostatic voltage curves (electrochemical oscillation) for surface-treated LTO anodes.[7] Interestingly, their experiment demonstrated that the electrochemical oscillation of the surface-treated LTO anode is due to the "collective electrochemical intercalation/deintercalation" within several-million active electrode particles participating in $Li_7Ti_5O_{12} \rightleftarrows Li_4Ti_5O_{12}$ phase separation. The authors attributed this electrochemical oscillation to the specific surface treatment and showed that carbon additions are necessary to observe this effect. However, the effects of carbon surface treatment, as well as the resultant high levels of rutile-TiO_2 as a phase impurity (19.55 wt%), were not explicitly discussed in this report.[7] More recently, the positive effect of a surface carbon coating layer on the phase transition kinetics of a similar two-phase transition battery material,

Y. Chen, H. Pan, C. Lin, J. Li, G. Zhao, J. Zhang, Y. Lin, Z. Huang
College of Physics and Energy
Fujian Provincial Key Laboratory of Quantum Manipulation and New Energy Materials
Fujian Normal University
Fuzhou 350117, China
E-mail: lijiaxin@fjnu.edu.cn; jmzhang@fjnu.edu.cn; zghuang@fjnu.edu.cn

Y. Chen, O. V. Kolosov
Physics Department
Lancaster University
Lancaster LA1 4YB, UK
E-mail: o.kolosov@lancaster.ac.uk

The ORCID identification number(s) for the author(s) of this article can be found under https://doi.org/10.1002/adfm.202105354.

DOI: 10.1002/adfm.202105354

Y. Chen, O. V. Kolosov
The Faraday Institution, Quad One
Harwell Science and Innovation Campus
Lancaster OX11 0RA, UK

H. Pan, C. Lin, J. Li
Fujian Provincial Engineering Technical Research Centre of Solar-Energy Conversion and Stored Energy
Fuzhou 350117, China

R. Cai, S. J. Haigh
Department of Materials
University of Manchester
Manchester M13 9PL, UK

G. Zhao, Y. Lin, Z. Huang
Fujian Provincial Collaborative Innovation Center for Advanced High-Field Superconducting Materials and Engineering
Fuzhou 350117, China

lithium iron phosphate (LFP), have been reported.[8] It was suggested that enhanced surface diffusion of lithium could play a key role in tuning the phase transformation in LFP electrodes.[9–11] These studies highlight that the importance of surface treatment for determining the electrochemical performance of phase-separation electrode materials like LFP/LTO cannot be overestimated, and a deeper investigation of underling mechanisms could rapidly accelerate battery development.

Setting up the appropriate validated model system is essential to reveal mechanistic insights in a multiparticle phase-separation system with mosaic instability.[12] Composite electrodes contains binders, conductive agents, as well as associated grain boundaries and interfaces. These will introduce additional complexity to the electrochemical oscillation behavior of the composite electrodes and could inhibit effective interpretation of the bulk effects of surface treatments. For our experimental model, we therefore chose to prepare binder and conductive additive-free LTO thin-film electrodes, as well as to introduce Al–ZnO (AZO) surface coatings to manipulate LTO electrode–electrolyte interfacial properties. It is also worth noting that, although a wide range of materials, including carbon,[13] Al_2O_3,[14] V_2O_3,[15] and ZnO/AZO,[16,17] have been tested as coating/decoration materials with the aim of improving deep-delithiated LTO (discharge cut-off voltage <1.0 V vs Li^+/Li) electrochemical performance, intensive debate remains regarding whether the coating layers retain the original chemistry or convert into a reduction protection layer with distinct physicochemical properties. In other words, apart from the bulk effect of phase-separation, the mechanism of how a thin coating layer on the LTO anode can increase the EEI interfacial stability and lithium transportation kinetics is not yet understood.

Operando characterization techniques with high-spatial/temporal resolution can overcome the limitations of static and destructive characterization methods, making them key to studying the nanoscale physical–chemical processes occurring in battery materials.[18] Using our LTO thin-film electrode as a model sample that effectively represents the electrode-coating layer-electrolyte multi-interface structure, in this work, we study the dynamic SEI formation processes in LTO electrodes with and without AZO coating by operando shear force modulation microscopy (SFMM) in a liquid electrolyte environment (see Figure S1 in the Supporting Information for detailed methods). We found that the coating layer transformed to an AZO-generated SEI layer consisting of compact Li–Zn alloy and Li_2O domains, which form a highly efficient ion-conducting matrix, while protecting the electrode surface from being decomposed by the electrolyte, thereby drastically improving the batteries cycling stability and rate performance. Benefiting from the high lithium-ion diffusion rate within this artificial AZO induced SEI layer, the reduced nucleation barrier then inhibits intrinsic electrochemical oscillation in the LTO thin-film electrode, resulting in the disappearance of voltage oscillation in the galvanostatic curves. Our results demonstrate that proper surface modification can not only modulate the surface conductivity and reductive capability, but also provide a major improvement of $Li_7Ti_5O_{12} \rightleftarrows Li_4Ti_5O_{12}$ phase transition kinetics for the electrode.

2. Results and Discussion

2.1. Electrode Structure Characterization

First, the bare LTO electrode material was prepared as well as similar samples where AZO was sputtered on the surface for 30, 60, and 90 s (referred to as AZO(30)–LTO, AZO(60)–LTO, and AZO(90)–LTO films, respectively). X-ray diffraction (XRD) patterns of the as-deposited and annealed bare LTO thin films are compared in **Figure 1**a. All the sharp diffraction peaks present for the as-deposited film are those of the stainless steel (SS) substrate, demonstrating that the as-deposited film is amorphous. After the annealing treatment, several additional diffraction peaks appear in the pattern, corresponding to the (111), (311), and (400) crystal planes of the cubic spinel LTO phase (JCPDS No. 49-0207). These diffraction data indicate the highly crystalline nature of the annealed LTO thin-film samples. The XRD patterns of the surface coated AZO(30)–LTO, AZO(60)–LTO, and AZO(90)–LTO films can be found in Figure S2 in the Supporting Information. Nevertheless, the existence of these thin AZO coating layers was confirmed by Raman spectroscopy and conductive atomic force microscopy (C-AFM), as shown in Figure S3 in the Supporting Information.

The microstructures of the LTO thin-film electrodes were further characterized using electron microscopy. Figure 1b,c shows scanning electron microscopy (SEM) images of the surface of the annealed LTO film and of the 60 s AZO decorated LTO (AZO(60)–LTO), respectively. A surface grain size of ≈70 nm is observed for the bare LTO (the grain size distribution statistics can be found in Figure S4a,b in the Supporting Information), and AZO(60)–LTO surface is covered by a coating layer with fine nanostructure after 60 s sputtering of AZO. The coating layer becomes more visible for longer sputtering times (Figure S6, Supporting Information). Energy dispersive X-ray spectroscopy (EDS) measurements in the SEM reveal an even distribution of Zn and Al on the AZO(60)–LTO sample surface (Figure S7, Supporting Information). To determine the thickness and crystal structures of the LTO and the AZO coating layer more precisely, high-resolution EDS and (scanning) transmission electron microscopy ((S)TEM) measurements were carried out for thin-film cross-sections prepared by focused ion beam (FIB) milling. Figure 1c shows scanning transmission electron microscope (STEM)-EDS elemental mapping of the AZO(60)–LTO film cross-section, where the thin Zn layer confirms the presence of AZO on the LTO surface (no Zn-layer signal can be observed in the bare LTO sample as shown in Figure S5 in the Supporting Information). The Fe and Pt elemental signals come from the SS substrate and the protective Pt surface layer required for FIB sample preparation, respectively. Figure 1e shows the cross-sectional high-resolution TEM (HR-TEM) image of the AZO(60)–LTO film where a grain size of ≈90 nm is visible in the LTO. The statistical distribution of grain sizes obtained from the cross-section HR-TEM (Figure S4c, Supporting Information) shows a slightly higher bulk grain size value comparing to the surface grain size analyzed by SEM. This may be due to interior grain growth during annealing of the LTO film. Figure 1f shows an enlarged view of the LTO–AZO interface, where the ≈10 nm thick amorphous AZO layer is visible atop of a polycrystalline LTO film. The AZO layer can be distinguished from the Pt protective coating

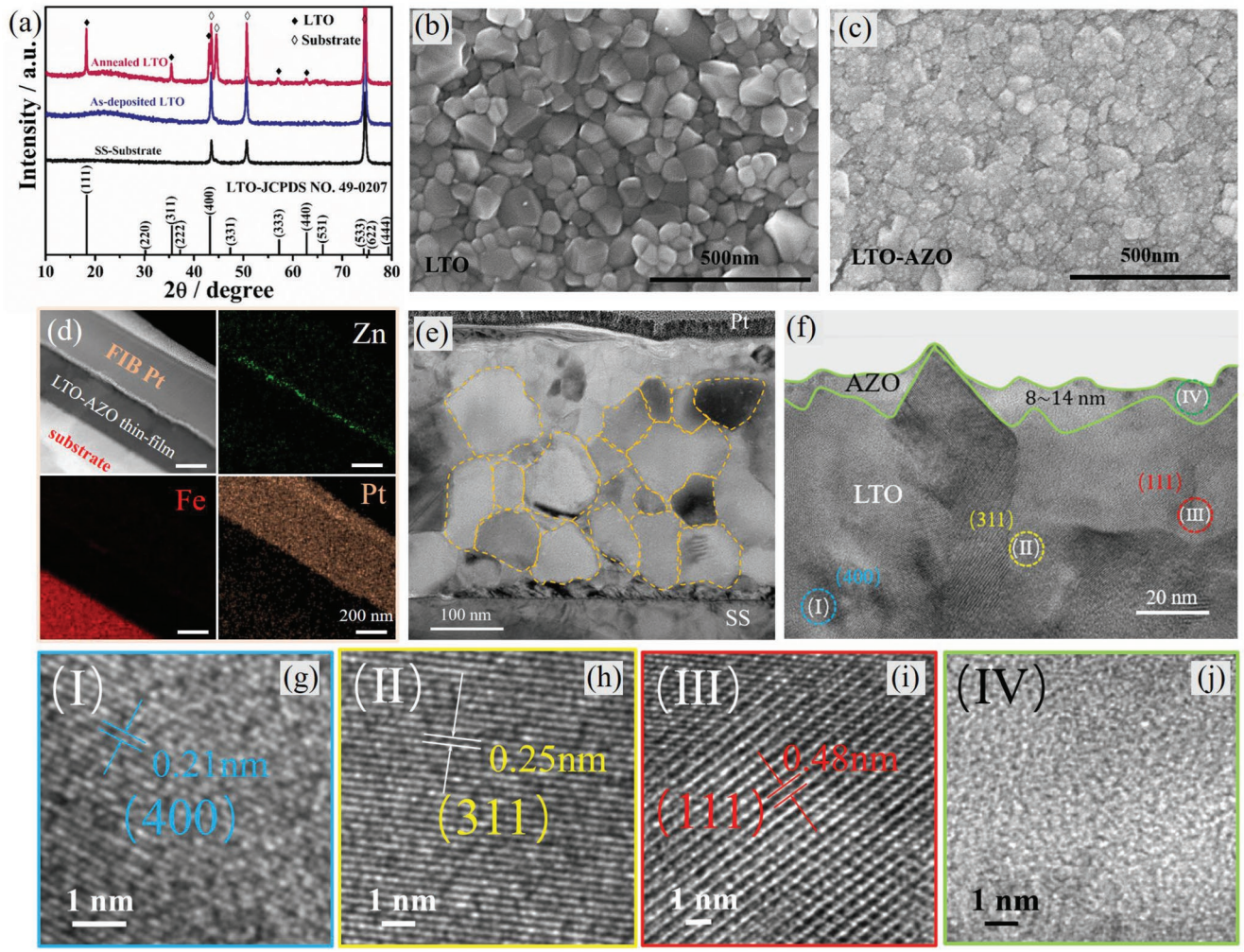

Figure 1. a) XRD patterns from the stainless steel (SS) substrate, the as-deposited bare LTO film, and the annealed LTO film. b) Secondary electron SEM images of the bare LTO film and c) AZO(60)–LTO film (representative SEM images for AZO(30)–LTO and AZO(90)–LTO samples can be found in Section S5 in the Supporting Information). Cross-sectional (S)TEM investigation of the AZO(60)–LTO film: d) HAADF-STEM image of AZO–LTO cut by FIB; f) HR-TEM image of the AZO(60)–LTO film with higher magnification view for the four dashed areas labeled I–IV indicated in panels (g)–(j); the Pt protective layer nanostructure and Zn element line scan is displayed in Section S5 and Figure S5a,b in the Supporting Information.

from the present of Zn in the ESD elemental map (Figure S5, Supporting Information). Analysis of the interplanar-spacings of each region in the LTO confirms the cubic spinal LTO phase (spacings of 0.48, 0.25, and 0.21 nm, correspond to the (111), (311), and (400) crystal planes, respectively). The selected area electron diffraction (SAED) patterns acquired from the LTO layer (Figure S8, Supporting Information) revealed crystalline diffraction rings which could be indexed to the expected LTO crystal planes. The absence of visible crystal structure in the AZO layer suggests this is amorphous. Overall, the structural characterization confirms the model structure of a polycrystalline LTO thin-film electrode, with an ultrathin amorphous AZO coating layer.

2.2. Electrochemical Performance

The electrochemical performance of the bare LTO and various AZO–LTO thin-film electrodes were evaluated using coin half cells. The details of thin-film areal capacity evaluations and calculations can be found in Section S6 in the Supporting Information. **Figure 2**a,b shows the cycling and rate performances of the bare LTO and AZO–LTO film electrodes at room temperature. From the figures, it can be found that the proper AZO surface modification has significant influence on the electrode's electrochemical performance. Especially, AZO(60)–LTO displays the best cycling performance. The pure LTO thin-film electrode has an initial capacity of 27.4 μAh cm^{-2}, while its reversible capacity gradually decreases to ≈17.8 μAh cm^{-2} over the first 100 cycles and then remains approximately stable. For AZO(30)–LTO, the cycling performance is similar to bare LTO, apart from a slightly higher initial capacity (30.6 μAh cm^{-2}) demonstrating that only 30 s of AZO sputtering does not make much of a difference to the LTO cycling performance. The decorated AZO coating on the AZO(30)–LTO electrode appears to form "nanoislands," aggregating in the "valleys" between LTO grains, rather than a uniform decoration layer (Figure S6,

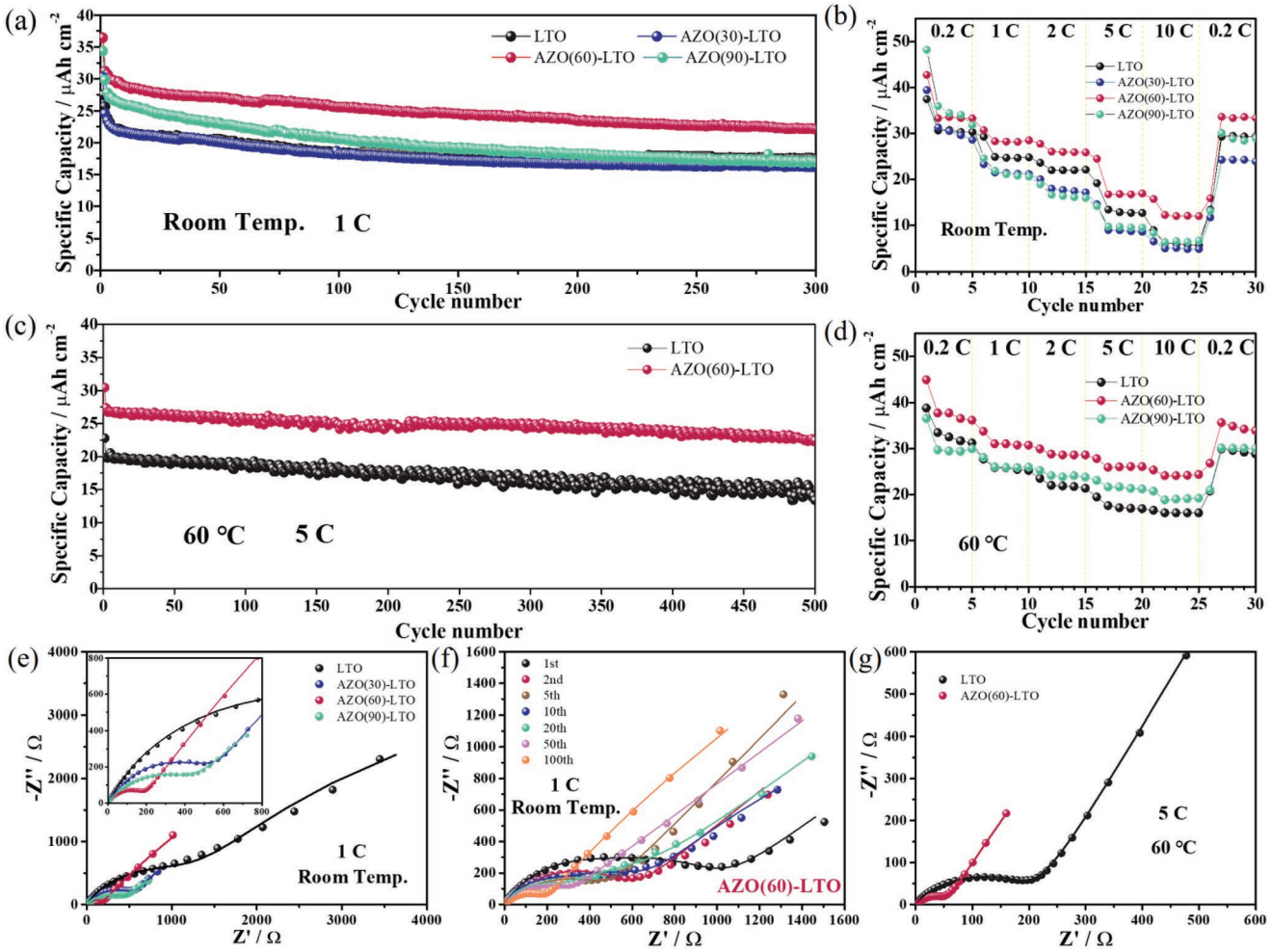

Figure 2. Cycling and rate performance of bare LTO, AZO(30)–LTO, AZO(60)–LTO, and AZO(90)–LTO between 0.1 and 3.0 V. a) Cycling performance at room temperature; b) rate performance at room temperature; c) cycling performance at 60 °C; d) rate performance at 60 °C; e) Nyquist plots of LTO and AZO–LTO thin-film electrodes after 100 cycles at 1C and room temperature; f) Nyquist plots of AZO(60)–LTO film electrode after different charge/discharge cycles and g) LTO film and AZO(60)–LTO film electrodes after 100 cycles at 5C and 60 °C.

Supporting Information). In this case, the AZO coating layer after reduction decomposition cannot form the continuous protective layer needed to effectively suppress the electrolyte decomposition, as well as to provide low charge transfer resistance. Therefore, the cycling performance and rate capability of AZO(30)–LTO is similar to the bare LTO. The AZO(90)–LTO film had an even higher initial capacity of over 33.4 μAh cm^{-2}, and then gradually decayed to ≈16.7 μAh cm^{-2} after 300 cycles. This high initial capacity derives from the electrochemically active AZO coating layer and the irreversible SEI formation,[19] as well as the surface lithium storage[20] that contributes to the extra initial Faraday capacity. However, a thicker AZO coating layer may not be able to be fully and uniformly reduced into the highly conductive Li–Zn/Li_2O/AlF_3 protection layer. Therefore, the charge transfer and ion diffusion through this inhomogeneous solid–liquid interface was reduced, resulting in a high charge transfer resistance. Moreover, upon cycling, inhomogeneous lithiation/delithiation states present on the AZO(90)–LTO film surface can generate local strain especially in low voltage range, potentially causing damage to the local crystal structure and surface relaxation,[21] with all these being detrimental to the electrode performance of AZO(90)–LTO. The AZO(60)–LTO shows the best cycling stability and is still able to deliver ≈22.3 μAh cm^{-2} after 300 cycles. The initial capacities of all AZO decorated LTO are higher than the bare LTO, indicating that the AZO coating partially contributes to the magnitude of the irreversible capacity during the first cycle.[22] Cyclic voltammetry measurements also confirm that a protective layer was formed on the electrode surface via the electrochemical decomposition of AZO, the so called "self-sacrificing effect" (see Figure S9 in the Supporting Information). Figure 2b shows the rate performances of the four samples at various charge/discharge rates (0.2C, 1C, 2C, 5C, and 10C). At 1C cycle rate, we find that the average capacity of the bare LTO film is ≈24.8 μAh cm^{-2}, and the average capacities of AZO(30)–LTO and AZO(90)–LTO films are slightly less than 22.3 μAh cm^{-2}; while the average capacity of the AZO(60)–LTO film can reach as high as 28.2 μAh cm^{-2}. Moreover, as the rate increases, the observed capacity of AZO(30)–LTO and AZO(90)–LTO become lower than bare LTO, while the capacity of AZO(60)–LTO

stays higher than bare LTO. The reduced rate performance of AZO(30)–LTO and AZO(90)–LTO is directly linked to their high charge transfer resistance at the electrode–electrolyte interfaces.

The electrochemical performances of the bare LTO and AZO decorated LTO was also studied in a high-temperature environment, in which lithium diffusion is activated and more serious electrolyte decompositions is commonly observed.[19] Figure 2c,d shows their cycling and rate performances between 0.1 and 3.0 V at 60 °C. The AZO(60)–LTO film shows good cycle stability at high temperature and high rate (5C). The specific capacity remains at 22.3 μAh cm^{-2} even after 500 cycles. By contrast, after 500 cycles, the bare LTO film delivers a specific capacity of just 13.4 μAh cm^{-2}. This high-temperature cycling performance degradation seen for these LTO films is similar to that observed previously for LTO composite electrodes due to electrolyte decomposition.[19] As shown in Figure 2d, comparing AZO(90)–LTO with the bare LTO samples reveals that their capacities are similar at low rates, but at high rates, AZO(90)–LTO delivers higher capacity. This indicates that uniform coating of the LTO surface with too thick an AZO layer may still resist the electrolyte decomposition at elevated temperature. However, AZO(60)–LTO displays the best rate performance at all charge/discharge rates, delivering capacities of ≈26.1 μAh cm^{-2} and ≈24.1 μAh cm^{-2} at 5C and 10C, respectively. Therefore, these results indicate that an AZO coating layer of appropriate thickness can improve the charge transfer and lithium diffusion, which results in better rate performances when cycling between 0.1 and 3.0 V both at room temperature and at elevated temperature. This could be attributed to the protection from an AZO-derived SEI layer, which prevents serious electrolyte decomposition on the electrode surface at elevated temperature.

Electrochemical impedance spectroscopy (EIS) measurements were next employed to understand the origin of the rate performance differences. The equivalent circuit model and lithium diffusion calculation details can be found in Figures S10 and S11 in the Supporting Information. Figure 2e,f shows the EIS of coin cells that contained bare LTO or AZO–LTO electrodes. All curves contain a semicircle reflecting the charge transfer process in the high-frequency region and a slant line corresponding to the lithium-ion diffusion process in the low-frequency region.[23] The electrolyte Ohmic resistance (R_e) relates to the intercept of the high-frequency region, and diameter of the semicircle is proportional to charge transfer resistance (R_{ct}).[24] It can be seen from Figure 2e that, after 100 cycles at room temperature, the R_{ct} values of all AZO–LTO samples were significantly lower than that of the bare LTO. Among them, the R_{ct} of the AZO(60)–LTO cell is the smallest (≈160 Ω), which indicates that the AZO coating suppresses the increase of impedance during cycling. In order to further understand the mechanism of this suppressed impedance increase, we carried out EIS tests in AZO(60)–LTO cells after different numbers of cycles. As shown in Figure 2f, with increasing cycle number, the charge transfer resistance of the electrode decreased continuously. This could be because of the gradual reduction and conversion of the initial AZO coating layer into an SEI layer with high ionic conductivity. EIS testing after cycling at 5C and 60 °C also showed similar results. As shown in Figure 2g, the R_{ct} of the AZO(60)–LTO electrode was only about 50 Ω, and the bare LTO electrode was more than four times higher than that value. The lower charge transfer resistance of AZO(60)–LTO at elevated temperature could be the reason for its better rate performance compared to bare LTO, as shown in Figure 2b. The EIS results show that the AZO coating reduces the charge transfer resistance of the cells, which is beneficial for the kinetics of electron and lithium-ion transportation within the cell, and therefore will result in a better cycle and rate performance. Based on the EIS data in Figure 2e, the chemical diffusion coefficient of Li^+ (D_{Li}^+) was calculated (see Section S6 in the Supporting Information for details). After 100 cycles at room temperature and 1C, the D_{Li}^+ of bare LTO, AZO(30)–LTO, AZO(60)–LTO, and AZO(90)–LTO electrodes are around 3.30×10^{-12}, 6.81×10^{-12}, 3.12×10^{-11}, and 9.12×10^{-12} cm^2 s^{-1}, respectively. In other words, the proper AZO coating layer can improve lithium-ion transportation, with the diffusivity being highest in AZO(60)–LTO, which showed a value nearly an order of magnitude higher than bare LTO.

2.3. SEI Formation and Compositional Analysis

EIS measurements show that the AZO(60)–LTO cell has initially high impedance before cycling, while the R_{ct} values dramatically decrease during the initial cycles (Figure 2f). The boosted charge transfer properties should relate to partial reduction of the AZO coating layers and consequential SEI formation. Real-space observation of the SEI formation in the liquid environment on both electrodes surface can provide direct evidence for this hypothesis. Operando AFM has demonstrated its versatility for the real-space observation of SEI formation in battery materials,[25] however, few reports have applied shear vibration interactions between the tip–sample, which is extremely sensitive to the viscoelastic SEI layer, to monitor the dynamic growth of SEI layers. We therefore first applied the operando SFMM technique here to monitor the initial dynamic SEI formation process on bare LTO and on the AZO(60)–LTO electrode surface. A detailed instrument sketch and explanation of the measurement principles is provided in Section S1 in the Supporting Information.

Figure 3 shows the operando SFMM measurements obtained for the LTO and AZO(60)–LTO samples. The shear force approach-retract spectra were recorded at different voltages during the first cyclic voltammetry (CV) cathodic scan. The Z piezo moved from 0 nm to the preset vertical deflection set-points, ramping the tip toward the sample surface. During ramping, the vertical displacement of the tip, as well as the lateral vibration phase were recorded simultaneously as reported elsewhere.[26,27] As can be seen in the 2D operando shear force spectra in Figure 3a, at open circuit potential (spectrum A), the torsion phase spectrum suddenly jumps from 90° to 0° as long as the tip was contacting the electrode surface (at around Z = 275 nm), indicating a clean surface without SEI. This "jumping" of the torsion phase can still be observed at a cathodic voltage around 1.6 V as shown in spectrum B, where regions I and II correspond to the electrolyte and LTO electrode, respectively. However, as the cathodic voltage is scanned down to around 0.75 V, a transition region in the phase approaching curves corresponding to an ≈90° phase shift, emerges as shown in spectra C and D in

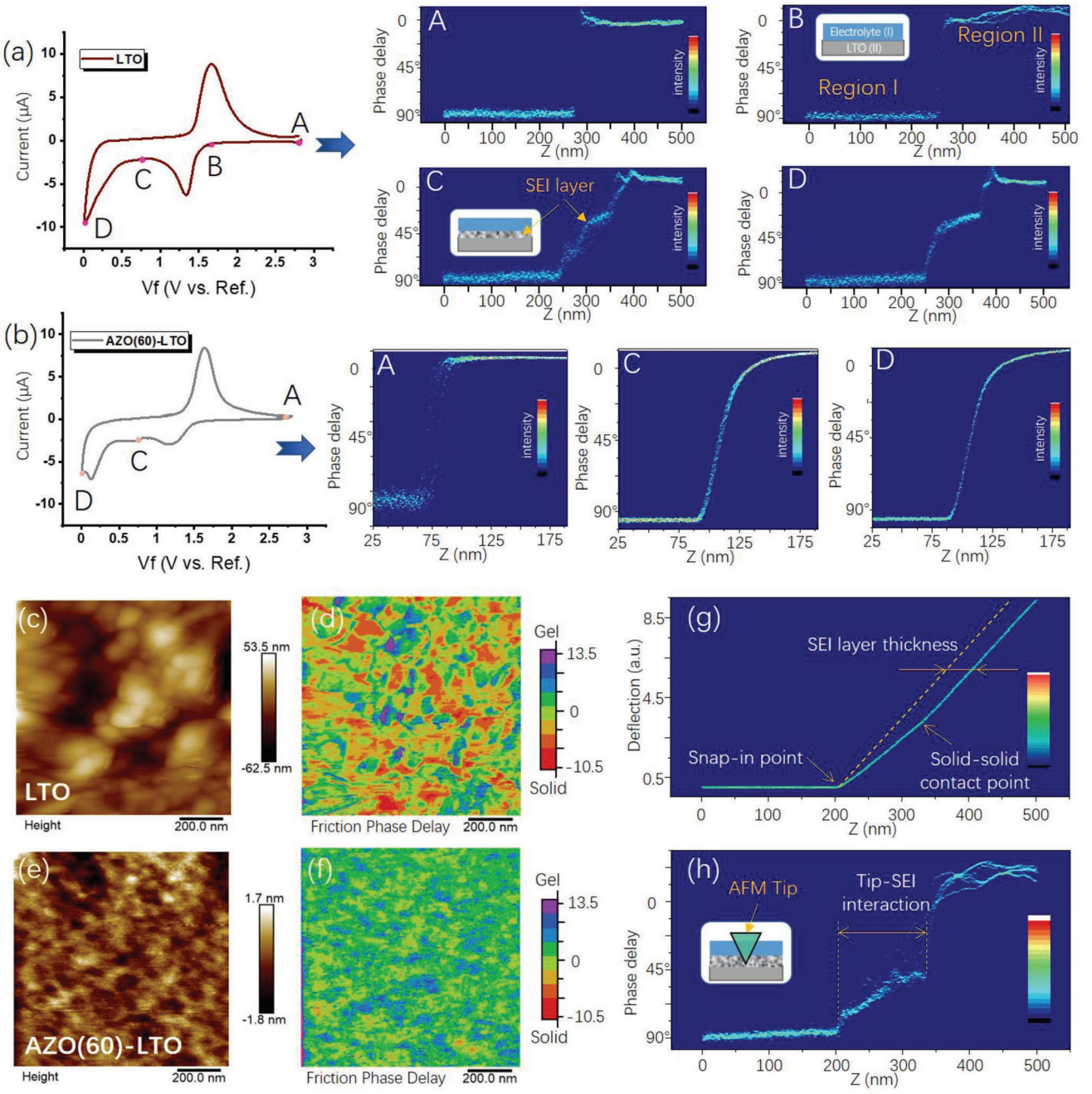

Figure 3. 2D operando shear force AFM spectra of a) bare LTO and b) AZO(60)–LTO thin-film electrodes at different cathodic voltages during the first CV cathodic scan (scan rate 0.5 mV s^{-1}, active material mass may vary due to the operando cell structure, measurement sample points: A = 2.8 V, B = 1.7 V, C = 0.75 V, and D = 0.1 V). c) The topography and d) torsional phase images of bare LTO after the first cathodic scan. e) The topography and f) torsional phase images of AZO(60)–LTO after the first cathodic scan. g) The vertical deflection versus piezo *Z* movement and h) the corresponding phase delay versus piezo *Z* movement.

Figure 3a. According to the phase delay analysis (Figure S1, Supporting Information), this should be attributed to the formation of viscous SEI layers on the solid LTO surface. Interestingly, one can find in **Figure 4**b that this significant "jumping" transition does not appear on the AZO(60)–LTO samples during the whole cathodic scan from open circuit potential (OCP) down to 0.1 V, indicating a dramatic difference of the tip-contact status compared to bare LTO. Immediately after the tip contacts the AZO(60)–LTO sample surface, the phase lag decreases with an increase of the vertical displacement (*Z*); similar trend was reported for solid–solid contact of the tip with silicon oxide.[28] In other words, the "missing" gel-like transition region in the torsion phase approaching spectra in the AZO(60)–LTO surface indicates the absence of a loose/viscous SEI layer formed on the electrode surface, indicating that the AZO(60)–LTO surface SEI layer is a mechanically stronger and stiffer surface passivation layer.

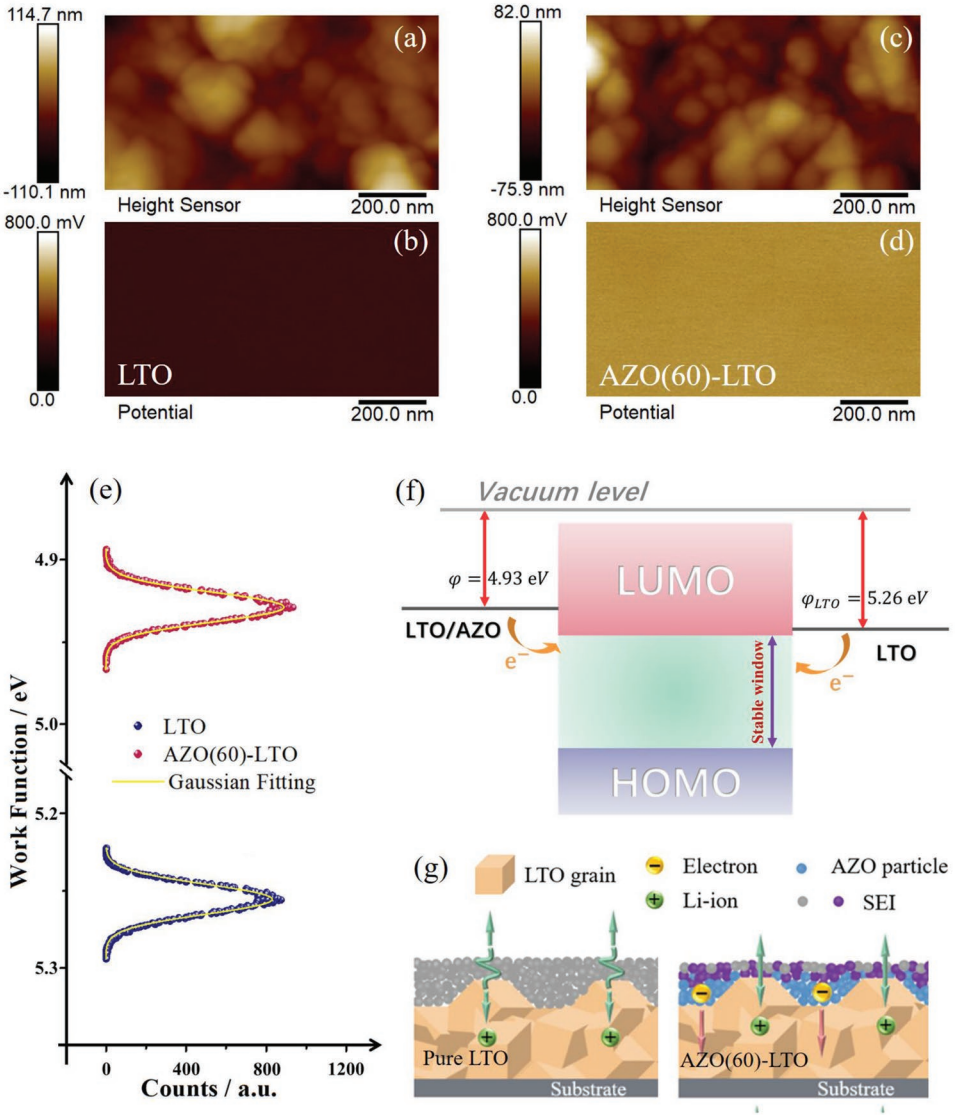

Figure 4. a) Surface morphologies and b) potential maps of bare LTO. c) Surface morphologies and d) potential maps of AZO(60)–LTO thin-film electrodes detected by KPFM. e) Effective work functions LTO films and AZO(60)–LTO films. f) Schematic energy diagrams of the electrode/electrolyte interfaces. g) SEI formation model on both electrode surfaces.

The homogeneity of the SEI formed on LTO and AZO(60)–LTO was further characterized by SFMM mapping with Figure 3c–f showing both the topography and phase images recorded simultaneously. By comparing Figure 3c with Figure 3e, one notices that the bare LTO surface shows a rough topography with many irregular SEI bumps, while the AZO(60)–LTO surface was covered by a smooth passivation layer with finer structure. Additionally, Figure 3d,f is the phase images, recording the same areas as in the topography images in Figure 3c,e, respectively. It is clear that LTO surface shows much more inhomogeneity in phase delay comparing to AZO(60)–LTO, which confirms that a more uniform SEI layer with more uniform chemical composition was obtained on the AZO modified LTO surface after the first cathodic scan, compared to the bare LTO. Figure 3g,h shows the vertical deflection and the corresponding torsional phase approaching spectra at the central position of Figure 3d. Two distinct regions with different slopes, corresponding to the tip-SEI indentation ($210 < Z < 340$ nm) and pure tip bending ($Z > 340$ nm) regions, can be observed in the deflection approaching spectra. These two regions also show distinct phase response as shown in Figure 3h. Furthermore, by processing the vertical deflection curves assuming that the tip deflection is equal to the sample displacement in the region of the solid–solid tip–sample contact ($Z > 340$ nm), the SEI thickness can be reliably determined by measuring the horizontal distance between the raw force-spectrum curves and the dashed line corresponding to the solid–solid contact, as shown in Figure 3g. The obtained SEI thickness is around 45 ± 5 nm at the center point in Figure 3c. Operando SFMM measurements in this report therefore allow direct visualization and quantification of the dynamic growth of SEI layers of the order of a few tens of nanometers thick, and to

identify inhomogeneity in SEI chemical components that have different viscosities. The components and chemical bonds of these distinct SEI layers were further evaluated by postmortem X-ray photoelectron spectroscopy (XPS) (see Figure S12 in the Supporting Information). It is found that the SEI layers formed on the bare LTO surface contain high proportions of organic species mixed with inorganic LiF/Li_2CO_3, while on the AZO(60)–LTO electrode surface, the AZO coating layers were converted into Li/Zn–F and Li_2CO_3 rich inorganic reduction products, resisting the formation of inorganic decomposition products. This is consistent with operando SFMM characterization that show a mechanically much more homogenous SEI layer on the AZO–LTO than was formed on the bare LTO electrode surface.

2.4. Suppressed Interfacial Reduction Kinetics (Surface Effect)

Here, we have demonstrated that the surface decoration of LTO electrodes with AZO metal oxide is an effective method for improving the electrode–electrolyte interface stability, which increases the batteries Coulombic efficiency and rate performance. Nevertheless, in order to implement these, we need to further investigate the underlying physical and chemical phenomenon. Our EIS, SFMM, and XPS characterization results above confirm that the AZO decoration layer can be electrochemically reduced to form a Li–Zn rich passivation layer, which has high lithium-ion conductivity and mechanical stiffness, assisting the uniform intercalation of lithium ions and inhibiting SEI film growth. Yet the question remains—how can this AZO coating layer spontaneously exhibit "self-sacrificing" behavior while also preventing further electrolyte decomposition?

The formation of the SEI at the anode–electrolyte interface is thermodynamically governed by the alignment of the reduction energy level ($-eE_{reduction}$) of the electrolyte molecules and the Fermi level of the anode surface.[29] The surface electronic structure of the anodic electrode, which determines the reduction kinetics of the electrolyte relative to the anode surface, has been proven to be a critical parameter determining SEI formation and composition.[30] Therefore, Kelvin probe force microscopy (KPFM) measurements were carried out to understand how the electrode material itself affects the EEI interfacial stability and formation of the SEI. Figure 4a–d shows the surface potential and nanomorphology of the AZO coated LTO and bare LTO films measured by KPFM. From these, it is found that the surface potential of the thin-film electrode (AZO(60)–LTO) was dramatically increased by the AZO coating compared to bare LTO. The effective work functions (EWFs) of each thin-film electrode were further calculated from these surface potential maps, and the distribution functions are presented in Figure 4e. It is shown that the EWF of the AZO(60)–LTO electrode (≈4.93 eV) is about 330 meV smaller than that of the bare LTO electrode (≈5.26 eV). According to the energy level diagram in Figure 4f, one can conclude that, compared to the bare LTO electrode surface, AZO(60)–LTO with a smaller EWF value has higher reduction kinetics on the anode–electrolyte interface, which could facilitate the reduction reactions occurring on the electrode surface[30] even before the electrochemical cycling begins. Therefore, during the initial discharge process, the anion and solvent adsorption species inside the inner Helmholtz layer[31] tend to react with the AZO coating layer rather than the LTO; while, at low lithiation voltage, AZO was further reduced creating an ionically conductive passivation layer consisting of Li–Zn nanoparticles embedded in the Li_2O matrix, and therefore dramatically improving the cycle and rate performances of the LTO anode. The SEI formation models are summarized in Figure 4g. This provides a clear explanation for the improved electrochemical performances observed in Figure 2, as well as the observed Li–Zn peaks in the XPS measurements (Figure S12, Supporting Information). The self-sacrificial behavior of the surface coating layer in anode materials is not unexpected[32,33] as the working potential window is relatively low when compared to the coating layers on the battery cathode side. It is well accepted that the oxide decoration layers on cathode materials are relatively stable and act as a physical barrier blocking the corrosion effects of HF in the electrolyte,[34] with the boosted charge transport processes in these coating layers being attributable to the built-in electric field derived from the coating layer-cathode heterojunction.[35] Interestingly, our experiments with AZO coated LTO anodes suggested that the "local built-in electric field" model[36,37] might be not suitable for metal oxide decorated anode materials because the decoration layer can be reduced electrochemically during cycling. It is also worth mentioning that some oxygen vacancies, which could improve ionic/electronic transport and ion insertion/extraction on the electrode–electrolyte interface,[38] might be generated on the LTO surface by the AZO coating. This could also contribute to the enhanced charge transfer capability of the AZO coated electrode.

2.5. Inhibited Electrochemical Oscillation (Bulk Effect)

Here, we explore the effects of the stabilized electrode–electrolyte interfacial structure on the phase-separation kinetics of the LTO electrodes. In a recent report on electrochemical oscillation of LTO, the observed voltage oscillation during galvanostatic charge/discharge has been attributed to a "group-by-group" phase transition path.[7,39] Since the "group-by-group" phase transition path represents the electrode-scale bulk inhomogeneities in lithiation/delithiation that are closely associated with the amplified local exchange current density, the presence of oscillations may indicate accelerated electrode performance degradation.[40] We therefore carefully examine the voltage oscillations in our LTO thin-film electrode model to better understand the effects of AZO surface treatment.

To discuss the electrochemical oscillations of LTO electrodes, it is instructive to first look at the lithiation/delithiation induced voltage response of a single-grain with a nonmonotonic chemical potential.[41,42] According to the regular solution model, the free energy of a homogenous phase transition for a single-grain can be described as[41,42]

$$F(c,T) = \Omega c(1-c) + k_B T\left[c\ln c + (1-c)\ln(1-c)\right] \quad (1)$$

where c is the lithium concentration in the LTO single-grain, k_B is Boltzmann constant, T is absolute temperature, and Ω is the

constant representing the nearest-neighbor interaction between lithium ions within the host lattice. The chemical potential $\mu(c)$ can be obtained by differentiating the free energy with respect to lithium concentration

$$\mu(c) = \Omega(1-2c) + k_B T \ln\left(\frac{c}{1-c}\right) \quad (2)$$

Therefore, the open circuit voltage V_{OCP} can be written as

$$V_{OCP} = V_{EQ} - \frac{\mu(c)}{e} \quad (3)$$

where V_{EQ} is equilibrium voltage and e is electron charge. In **Figure 5**a, the red-dashed line shows the simulated open circuit voltage profiles based on Equation (3). It is clearly that when entering the two-phase region, the filling/extraction of lithium-ions in a LTO single-grain will result in the observed "bump" in the galvanostatic voltage curve (green solid line) overshooting the two-phase equilibrium voltage (black dashed horizonal line). This voltage bump is a fundamental feature of the electrochemical oscillation phenomenon. Thus, extending this voltage bump phenomenon to a scenario where there are many particles, as shown in Figure 5b, the phase separation will follow a one-by-one pathway due to the "mosaic instability," and thereby the galvanostatic voltage profile may exhibit many sudden rises and drops due to the sequential mosaic instability events.[39,42]

However, for commercial LTO/LFP composite electrodes (consisting of about $\approx 10^{10}$–10^{9} grains), the localized mosaic instability events randomly occur over the whole electrode during the charge/discharge and this smooths out the voltage bumps. As a result, a flat voltage plateau is usually observed in the two-phase regime of these multiparticle phase-separation composite electrodes.

Therefore, it is important to note that the voltage oscillations emerge only when the mosaic instability events occur discretely separated in time and space upon galvanostatic charge/discharge. Specifically, as shown in Figure 5c, during discharge, the phase separation concurrently occurs at each "group" of active crystal-grains (such as the N_α group or $N_{\alpha+1}$ group) when the voltage oscillations reach each peak/valley. This "group-by-group" model is a more realistic scenario consistent with experimental observations.[43,44]

As shown in Figure 5d, in the LTO thin-film anode, voltage oscillation was observed in both galvanostatic charge/discharge platforms during the initial cycling, while this oscillation disappears outside of the charge/discharge platforms (Figure S13, Supporting Information). The oscillation signals on the charge/discharge platforms show a slightly increased amplitude after the first cycle, but almost identical frequency (period). This voltage oscillation can be attributed to the discrete nature of multiparticle phase-separated reactions as discussed above. The fraction of actively phase-separating particles (Δgrains) can be further estimated by analyzing the charge/discharge voltage

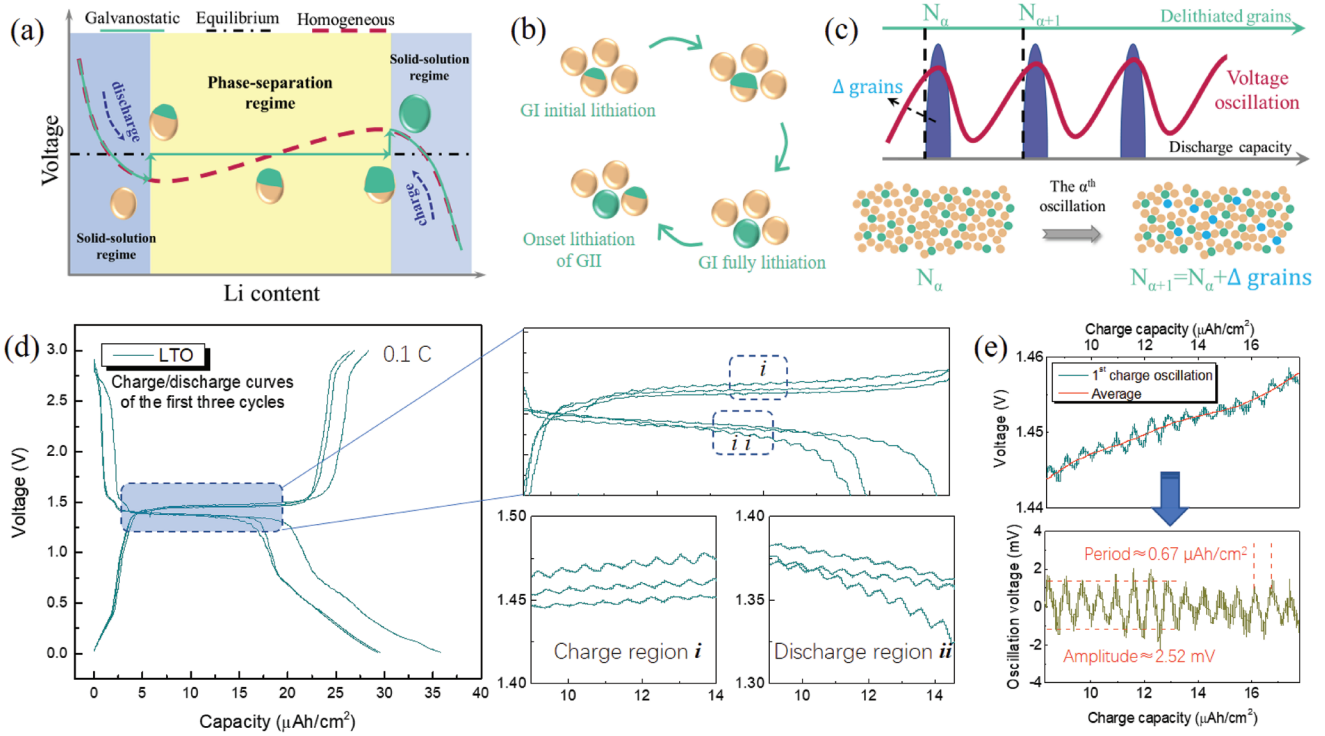

Figure 5. a) The proposed open circuit voltage profiles of galvanostatic discharge and homogeneous lithiation in a single-grain. The galvanostatic process is the green solid line and the hypothesized homogeneous lithiation/delithiation process is represented by the red dashed line, and the two-phase equilibrant voltage is the black dashed horizontal center line. b) The voltage bump mechanism in a system with multiple particles due to the "mosaic instability," the onset lithiation of grain II (GII) happens only when grain I (GI) is fully lithiated. c) The phase-separation occurs with certain active percentages of grains in the "group-by-group model" (Δgrains is the number of active grains/particles in each oscillation). d) Electrochemical oscillation phenomenon seen in the galvanostatic charge/discharge curves of LTO samples at 0.1C and e) oscillation period and amplitude analysis.

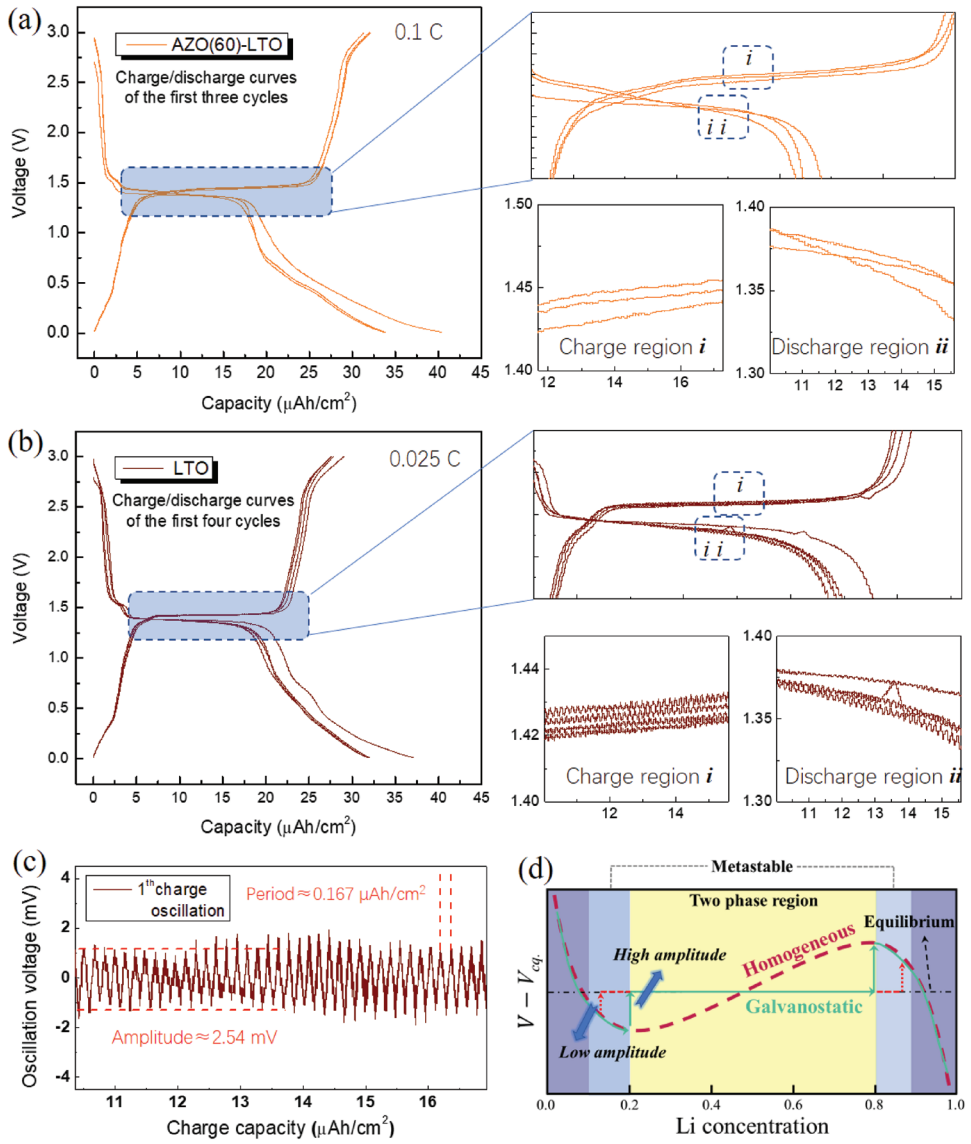

Figure 6. a) Galvanostatic charge/discharge curves of AZO coated LTO samples at 0.1C. b) Electrochemical oscillation phenomenon in bare LTO sample at low charge/discharge current density (0.025C) and c) oscillation period and amplitude analysis. d) Relation between lithium diffusion (redistribution capability) and electrochemical oscillation amplitudes.

oscillation curves. As shown in Figure 5e, by subtracting the average line of the first charge, the obtained flattened oscillation signal shows an amplitude of about 2.52 mV and a period about 0.67 μAh cm^{-2}. Therefore, the estimated fraction of actively phase-separation particles is about 2.3%. Assuming a uniform grain-size distribution within the thin-film electrode, the estimated number of crystal grains in a LTO thin-film electrode is around $\approx 10^{10}$. Since the oscillating period (in capacity) is proportional to the number of active grains, each "group" includes about $\approx 2.3 \times 10^8$ grains, indicating that the collective phase separation of numerous grains in the LTO thin-film electrode is highly ordered. However, as shown in **Figure 6**a–c, the oscillation behavior sensitively depends on the surface coating layer and intercalation/deintercalation rate.

As shown in Figure 6a, during the initial cycles, the AZO(60)–LTO does not show visible oscillation signals with a similar amplitude as LTO. As discussed in the operando SFMM and postmortem XPS characterization sections, the self-sacrificing AZO coating produced a robust SEI layer with high conductivity which could accelerate the ion transportation and charge transfer on the EEI. This may be the reason why voltage oscillations cannot be observed in the AZO(60)–LTO electrode. The high electronic conductivity of the AZO coating layer and ionically conductive SEI layer benefits charge transportation and Li^+ accumulation and the consequent lithium surface nucleation, which will trigger phase separation to enter the "metastable region" ahead of the unstable phase-separation regime as shown in Figure 6d.[7,11] As a result, not only the voltage bump was restrained in each single-grain (oscillation amplitude reducing), but the localized mosaic instability was also smoothed (periodicity destroyed or largely extended) over the whole thin-film

electrode. By contrast, the LTO electrode forms a thick surface passivation layer, which reduces the lithium "wetting effect" on the grain surface and therefore postpones the electrode entering metastable phase-separation region, resulting in a "higher oscillation amplitude" fluctuation in the galvanostatic voltage curves as soon as it reaches the inflection point. This is also the reason why voltage oscillations were observed in the surface treated LTO samples with high proportion of impurity in ref. [7], but disappeared in the AZO surface coated LTO in this study. The better surface lithium wetting effect in impurity-free LTO (reported in ref. [7]) and the AZO decorated LTO thin-film electrode reported here can both facilitate nucleation events on the LTO particle surface, as well as the rapid redistribution of electrons/lithium ions between the nanograins,[11] therefore inhibiting the electrochemical oscillations. It also worth noting that the voltage oscillation disappeared in the AZO(60)–LTO electrode even at the first lithiation voltage platform, where the AZO-derived SEI is not fully formed on the electrode surface. Whether the disappearance of the oscillations shown here is related to the enhanced lithium-ion de-solvation processes or precycle surface passivation layer needs to be further studied.

Compared to the electrochemical oscillation in ref. [7], the significant difference seen in this study is the ratio of the no-oscillation region versus oscillation region in charge/discharge voltage platforms. In our study, voltage oscillation was observed during the whole phase-separation region, while the oscillation only began at the later part of the two-phase region for the previous report.[7] Interestingly, a simple calculation shows that the estimated initial total grain numbers in each LTO electrodes are of the order of $\approx 10^{10}$, which is at the same order as the onset of oscillation for the electrode grains/particles in ref. [7]. We therefore believe that, in our LTO thin-film electrode, the grain number is small enough for stochastic fluctuation of mosaic instability events to induce the oscillatory phenomenon even at the initial phase-separation region (the beginning of charge/discharge voltage platforms). This also explains the electrochemical oscillation caused by the less active grains at low charge/discharge rate as shown in Figure 6b,c. From Figure 6c, it can be found that the voltage oscillation frequency of the bare LTO electrode was increased at lower charge/discharge rates. The reduced active grain friction (fewer active grains) during the entire phase-transition is enough to deliver the required galvanostatic charge/discharge current at lower rate cycling, leading to diminished the electrochemical oscillation period in the LTO electrode at lower charge/discharge rates.

Based on the electrochemical performance summarized in Figure 2 and confirmed by electrochemical oscillation analysis, it is clear that the properly surface treated LTO thin-film electrode which does not exhibit electrochemical oscillations has better long-term cycling stability, rate performance, and improved charge transfer. Thus, we suggest that the observed electrochemical oscillations provide a key indicator that can be used to evaluate the lithium-ions transportation/redistribution capability and phase separation kinetics in a multiparticle system, as well as to directly reveal bulk electrode-scale inhomogeneities. Nevertheless, it should be noted that the effects of the partially irreversible insulator-to-metal phase transition ($Li_4Ti_5O_{12} \rightarrow Li_7Ti_5O_{12}$) during the first discharge has not been considered in this work. The residual metallic $Li_7Ti_5O_{12}$ phase could also boost the rapid redistribution of both Li^+ and electrons among/inside the electrode grains,[45,46] and thereby inducing phase-separation out of the equilibrium path. Additionally, the local accumulation of strain/defect at crystal grain boundaries has been observed to generate strain-enhanced ion/electrode transportation channels.[47,48] Since the grain boundary density of the polycrystalline LTO thin-film electrode is higher than the LTO composite electrode, complete understanding of the interplay between electrochemical oscillations and battery performance should also include the consideration of the grain boundaries. These fundamental scientific issues underpin the success or failure of surface coating techniques for improving the performance of phase separation LIB materials yet they are not well understood. Both the effects of AZO surface coatings on discrete phase-separating behavior in a multiparticle LTO composite electrodes, and the correlation of this surface coating with near surface crystal structure relaxation,[21] require further in-depth studies.

3. Conclusions

To elucidate the critical role of surface modification layers on the batteries electrochemical performance, LTO thin-film electrodes with and without AZO nanocoating layers were constructed as experimental models to study of the underlying mechanisms of performance improvement. The effects of the self-sacrificing AZO modification layer on the electrochemical performance of deep-delithiated LTO thin-film electrodes were studied. We show that the electrochemical reaction between Li and AZO during initial discharge/charge process generates an efficient and high performance artificial SEI protection layer. The nanomechanics and chemical compositions of this SEI layer were characterized using advanced operando SFMM spectra and postmortem XPS, which confirms that in AZO(60)–LTO this thin SEI layer is highly homogeneous, mainly consisting of stiff, high elastic moduli and negligible viscosity inorganic components (Li–Zn alloy, Li_2CO_3, and LiF). This artificial inorganic SEI layer has high ionic conductivity, protecting the electrode surface from electrolyte decomposition, and therefore dramatically improving the cycling and rate performance of the LTO anode. KPFM measurements suggested that the suppressed reduction kinetic on the EEI is key for the initial formation of the "self-sacrificing" SEI layer. Most importantly, by introducing this artificial SEI layer, we also demonstrate that surface modifications can not only modulate the surface conductivity and reductive capability, but also improve $Li_7Ti_5O_{12} \rightleftarrows Li_4Ti_5O_{12}$ phase transition kinetics through inhibiting the intrinsic electrochemical oscillations. This unambiguously suggests that the surface lithium wetting effect, as well as the rapid redistribution of lithium ions between the nanograins are critical factors for the observation of electrochemical oscillations. Importantly, we attributed the enhanced electrochemical performance of the surface modified LTO electrodes to the suppressed electrochemical oscillations, which represents a more homogenous local exchange current

and intercalation/deintercalation states within the electrodes. This work highlights the importance of in-depth understanding of the enhancement mechanisms for electrode surface coatings in batteries, as well as filling an important gap between experimental observations and fundamental understanding of Li intercalation in multiparticle-phase-separating systems.

4. Experimental Section

Thin-Film Electrode Preparations: LTO thin-film electrodes were deposited using RF magnetron sputtering. The deposition chamber was evacuated using a turbo-molecular pump to an initial pressure of 4×10^{-4} Pa, and the sample/target distance was fixed at 10 cm. LTO thin-film electrodes were deposited onto SS substrates with a diameter of 15.5 mm. During the deposition, the substrate temperature was kept at room temperature; the chamber pressure was maintained at 1.0 Pa. The gas flow rate was set at 50 sccm with $Ar:O_2 = 4:1$. The sputtering was conducted at a power of 120 W for 8 h. After deposition, the LTO thin films were in situ annealed at 700 °C for 2 h. A ZnO target with a 2% aluminum doping rate was chosen as the modification material. While ZnO is a wide-bandgap semiconductor with low conductivity, its resistance is dramatically reduced by n-type aluminum doping. Additionally, besides the highly ionically conductive Zn–F phase, the byproduct, AlF_3, deriving from the AZO coating layer, could also improve the lithium interface compatibility, and therefore enhancing the long-term cycling stability. AZO modification layers were directly deposited onto the annealed LTO thin-films surface under a sputtering pressure of 0.5 Pa and a flow rate of 22 sccm. The AZO layer thickness was controlled by varying the deposition times (30, 60, and 90 s), and the obtained composite AZO/LTO films were labeled as AZO(30)–LTO, AZO(60)–LTO, and AZO(90)–LTO, respectively.

Thin-Film Structure Characterizations: The sample crystal structures were determined by XRD (Rigaku Ultima IV, Cu $K_{\alpha 1}$ radiation, $\lambda = 0.15406$ nm) and Raman spectroscopy. The surface compositions were analyzed by X-ray photoelectron spectrometer (Thermo ESCALAB XI+). The surface and cross-section morphologies were characterized by SEM (Hitachi SU-8010) and STEM (FEI Titan G2 80-200). STEM-EDS mapping was used to confirm the elemental distributions. AFM-based measurements were carried out in Bruker Dimension Icon and Multimode. KPFM was used to measure the sample effective work function. Nanoelectronic properties of LTO, AZO(30)–LTO, AZO(60)–LTO, and AZO(90)–LTO were measured by C-AFM. Operando SFMM was performed using advanced vibration modulated mode[49–51] on a homemade ultrasonic SPM cell, as illustrated in Figure S1 in the Supporting Information.

Electrochemical Measurements: Annealed LTO and AZO–LTO composite thin films were assembled into 2025 coin-cells as the working electrodes. The calculation of the capacity contribution from the AZO coating layers can be found in Section S6 in the Supporting Information. Li foils were chosen as the reference/counter electrodes. 1 M $LiPF_6$ in the mixture solution of ethylene carbonate (EC), diethyl carbonate (DEC), and dimethyl carbonate (DMC) (1:1:1 vol%) was used as the electrolyte. The half cells were charged/discharged at constant current using LAND CT2001A battery testing system with the cut-off voltages of 0.1–3.0 V at room temperature and 60 °C. CV tests were performed using an electrochemical workstation (Arbin Instruments BT2000, USA) with a scanning rate of 0.1 mV s^{-1}. The EIS were measured using a Zahner Zennium IM6 electrochemical workstation in the frequency range of 100 mHz to 100 kHz.

Supporting Information

Supporting Information is available from the Wiley Online Library or from the author.

Acknowledgements

Y.C. and H.P. contributed equally to this work. The authors wish to acknowledge the financial support by the National Natural Science Foundations of China (No. 61574037), the Fujian Natural Science Foundation for Distinguished Young Scholars (Grant No. 2020J06042), the Natural Science Foundation of Fujian Province (Grant No. 2018J01660), the Faraday Institution (grant number FIRG018), the EU Graphene Flagship Core 3 project, and the EPSRC projects EP/V00767X/1 and EP/P009050/1. This work was supported by the Henry Royce Institute for Advanced Materials, funded through EPSRC grants EP/R00661X/1, EP/S019367/1, EP/P025021/1, and EP/P025498/1.

Conflict of Interest

The authors declare no conflict of interest.

Data Availability Statement

Research data are not shared.

Keywords

electrochemical oscillation behavior, lithium battery performance, lithium titanate thin-film electrode, operando shear force spectroscopy, surface decoration engineering

Received: June 4, 2021
Revised: July 17, 2021
Published online:

[1] X. Yu, A. Manthiram, *Energy Environ. Sci.* **2018**, *11*, 527.
[2] C. Yan, R. Xu, Y. Xiao, J. F. Ding, L. Xu, B. Q. Li, J. Q. Huang, *Adv. Funct. Mater.* **2020**, *30*, 1909887.
[3] G. Sun, C. Zhao, F. D. Yu, R. Yu, J. Wang, J. Zhou, G. Shao, X. Sun, Z. B. Wang, *Nano Energy* **2021**, *79*, 105459.
[4] K. Pan, L. Zhang, W. Qian, X. Wu, K. Dong, H. Zhang, S. Zhang, *Adv. Mater.* **2020**, *32*, 2000399.
[5] K. M. Colbow, J. R. Dahn, R. R. Haering, *J. Power Sources* **1989**, *26*, 397.
[6] S. Scharner, W. Weppner, P. Schmid-Beurmann, *J. Electrochem. Soc.* **1999**, *30*, 857.
[7] D. Li, Y. Sun, Z. Yang, L. Gu, Y. Chen, H. Zhou, *Joule* **2018**, *2*, 1265.
[8] A. R. Iarchuk, V. A. Nikitina, E. A. Karpushkin, V. G. Sergeyev, E. V. Antipov, K. J. Stevenson, A. M. Abakumov, *ChemElectroChem* **2019**, *6*, 5090.
[9] Y. Li, H. Chen, K. Lim, H. D. Deng, J. Lim, D. Fraggedakis, P. M. Attia, S. C. Lee, N. Jin, J. Moškon, Z. Guan, W. E. Gent, J. Hong, Y. S. Yu, M. Gaberšček, M. S. Islam, M. Z. Bazant, W. C. Chueh, *Nat. Mater.* **2018**, *17*, 915.
[10] L. Savignac, J. M. Griffin, S. B. Schougaard, *J. Phys. Chem. C* **2020**, *124*, 7608.
[11] P. Bai, D. A. Cogswell, M. Z. Bazant, *Nano Lett.* **2011**, *11*, 4890.
[12] K. Y. Park, J. Hong, W. M. Seong, J. J. Kim, K. Ku, B. Lee, K. Kang, *Energy Environ. Sci.* **2017**, *10*, 2352.
[13] Y. B. He, F. Ning, B. Li, Q. S. Song, W. Lv, H. Du, D. Zhai, F. Su, Q. H. Yang, F. Kang, *J. Power Sources* **2012**, *202*, 253.
[14] D. Ahn, X. Xiao, *Electrochem. Commun.* **2011**, *13*, 796.
[15] D. Lei, H. Ye, C. Liu, D. An, J. Ma, W. Lv, B. Li, F. Kang, Y. B. He, *ACS Appl. Mater. Interfaces* **2019**, *11*, 29993.

[16] Y. Jin, H. Yu, Y. Gao, X. He, T. A. White, X. Liang, *J. Power Sources* **2019**, *436*, 226859.
[17] Y. Wang, Y. Ren, X. Dai, X. Yan, B. Huang, J. Li, *R. Soc. Open Sci.* **2018**, *5*, 180762.
[18] W. Li, D. M. Lutz, L. Wang, K. J. Takeuchi, A. C. Marschilok, E. S. Takeuchi, *Joule* **2020**, *5*, 77.
[19] F. Huang, J. Ma, H. Xia, Y. Huang, L. Zhao, S. Su, F. Kang, Y. B. He, *ACS Appl. Mater. Interfaces* **2019**, *11*, 37357.
[20] S. Ganapathy, M. Wagemaker, *ACS Nano* **2012**, *6*, 8702.
[21] H. C. Chiu, X. Lu, J. Zhou, L. Gu, J. Reid, R. Gauvin, K. Zaghib, G. P. Demopoulos, *Adv. Energy Mater.* **2017**, *7*, 1601825.
[22] H. Q. Dai, H. Xu, Y. N. Zhou, F. Lu, Z. W. Fu, *J. Phys. Chem. C* **2012**, *116*, 1519.
[23] Z. Lin, Y. Yang, J. Jin, L. Wei, W. Chen, Y. Lin, Z. Huang, *Electrochim. Acta* **2017**, *254*, 287.
[24] J. Deng, Z. Lu, C. Y. Chung, X. Han, Z. Wang, H. Zhou, *Appl. Surf. Sci.* **2014**, *314*, 936.
[25] H. Pan, Y. Chen, W. Pang, H. Sun, J. Li, Y. Lin, O. Kolosov, Z. Huang, *MethodsX* **2021**, *8*, 101250.
[26] B. A. Smith, B. Tolloczko, J. G. Martin, P. Grutter, *Biophys. J.* **2005**, *88*, 2994.
[27] K. Yamanaka, H. Ogiso, O. Kolosov, *Jpn. J. Appl. Phys.* **1994**, *33*, 3197.
[28] O. Piétrement, M. Troyon, *Surf. Interface Anal.* **2001**, *31*, 1060.
[29] P. Peljo, H. H. Girault, *Energy Environ. Sci.* **2018**, *11*, 2306.
[30] W. Song, E. S. Scholtis, P. C. Sherrell, D. K. Tsang, J. Ngiam, J. Lischner, S. Fearn, V. Bemmer, C. Mattevi, N. Klein, F. Xie, D. J. Riley, *Energy Environ. Sci.* **2020**, *13*, 4977.
[31] C. Yan, H. R. Li, X. Chen, X. Q. Zhang, X. B. Cheng, R. Xu, J. Q. Huang, Q. Zhang, *J. Am. Chem. Soc.* **2019**, *141*, 9422.
[32] B. Zhu, N. Liu, M. McDowell, Y. Jin, Y. Cui, J. Zhu, *Nano Energy* **2015**, *13*, 620.
[33] Q. Li, H. Pan, W. Li, Y. Wang, J. Wang, J. Zheng, X. Yu, H. Li, L. Chen, *ACS Energy Lett.* **2018**, *3*, 2259.
[34] J. Qian, L. Liu, J. Yang, S. Li, X. Wang, H. L. Zhuang, Y. Lu, *Nat. Commun.* **2018**, *9*, 4918.
[35] X. Ran, J. Tao, Z. Chen, Z. Yan, Y. Yang, J. Li, Y. Lin, Z. Huang, *Electrochim. Acta* **2020**, *353*, 135959.
[36] Y. Liu, T. Zhou, Y. Zheng, Z. He, C. Xiao, W. K. Pang, W. Tong, Y. Zou, B. Pan, Z. Guo, Y. Xie, *ACS Nano* **2017**, *11*, 8519.
[37] Q. Li, Y. H. Zhao, H. D. Liu, P. D. Xu, L. T. Yang, K. Pei, Q. W. Zeng, Y. Z. Feng, P. Wang, R. C. Che, *ACS Nano* **2019**, *13*, 11921.
[38] S. S. Li, X. B. Zhao, Y. Z. Feng, L. T. Yang, X. F. Shi, P. D. Xu, J. Zhang, P. Wang, M. Wang, R. C. Che, *Small* **2019**, *15*, 1901343.
[39] B. Orvananos, T. R. Ferguson, H. C. Yu, M. Z. Bazant, K. Thornton, *J. Electrochem. Soc.* **2014**, *161*, A535.
[40] C. Tian, Y. Xu, D. Nordlund, F. Lin, J. Liu, Z. Sun, Y. Liu, M. Doeff, *Joule* **2018**, *2*, 464.
[41] B. C. Han, A. Van der Ven, D. Morgan, G. Ceder, *Electrochim. Acta* **2004**, *49*, 4691.
[42] W. Dreyer, J. Jamnik, C. Guhlke, R. Huth, J. Moškon, M. Gaberšček, *Nat. Mater.* **2010**, *9*, 448.
[43] W. C. Chueh, F. El Gabaly, J. D. Sugar, N. C. Bartelt, A. H. McDaniel, K. R. Fenton, K. R. Zavadil, T. Tyliszczak, W. Lai, K. F. McCarty, *Nano Lett.* **2013**, *13*, 866.
[44] Y. Li, F. El Gabaly, T. R. Ferguson, R. B. Smith, N. C. Bartelt, J. D. Sugar, K. R. Fenton, D. A. Cogswell, A. L. D. Kilcoyne, T. Tyliszczak, M. Z. Bazant, W. C. Chueh, *Nat. Mater.* **2014**, *13*, 1149.
[45] C. Kim, N. S. Norberg, C. T. Alexander, R. Kostecki, J. Cabana, *Adv. Funct. Mater.* **2013**, *23*, 1214.
[46] M. S. Song, A. Benayad, Y. M. Choi, K. S. Park, *Chem. Commun.* **2012**, *48*, 516.
[47] L. T. Yang, X. Z. Zhu, X. H. Li, X. B. Zhao, K. Pei, W. B. You, X. Li, Y. J. Chen, C. F. Lin, R. C. Che, *Adv. Energy Mater.* **2019**, *9*, 1902174.
[48] W. L. Jiao, C. Chen, W. B. You, X. R. Zhao, J. Zhang, Y. Z. Feng, P. Wang, R. C. Che, *Adv. Energy Mater.* **2020**, *10*, 1904072.
[49] B. J. Robinson, M. E. Pumarol, O. V. Kolosov, *Phys. Rev. B* **2019**, *100*, 235426.
[50] B. J. Robinson, N. D. Kay, O. V. Kolosov, *Langmuir* **2013**, *29*, 7735.
[51] O. V. Kolosov, M. R. Castell, C. D. Marsh, G. A. D. Briggs, T. I. Kamins, R. S. Williams, *Phys. Rev. Lett.* **1998**, *81*, 1046.